Enhancing electrostrictive actuation via strong electrostatic repulsion among field-induced nanodomains in a relaxor ferroelectric poly(vinylidene fluoride-*co*-trifluoroethylene-*co*-chlorotrifluoroethylene) random terpolymer

Zhiwen Zhu[1,#], Guanchun Rui[2,#], Ruipeng Li[3], Hezhi He[1,*], Lei Zhu[2,*]

[1] *National Engineering Research Center of Novel Equipment for Polymer Processing, Guangdong Provincial Key Laboratory of Technique and Equipment for Macromolecular Advanced Manufacturing, South China University of Technology, Guangzhou, 510641, P. R. China*

[2] *Department of Macromolecular Science and Engineering, Case Western Reserve University, Cleveland, Ohio 44106-7202, United States*

[3] *National Synchrotron Light Source II, Brookhaven National Laboratory, Upton, New York 11973, United States*

# These authors contribute equally to this work.

* Corresponding authors. Emails: lxz121@case.edu (L. Zhu) and pmhzhe@scut.edu.cn (H. He)

Abstract

Electrostrictive polymers having a large strain are desirable for actuators, sensors, and energy harvesting in wearable electronics and soft robotics. However, a high electric field (>100 MV/m) is usually required for current electrostrictive polymers. To realize large electrostriction at reduced electric fields, the fundamental electrostriction mechanism needs to be better understood. In response to this need, the structure and electrostrictive properties of relaxor ferroelectric poly(vinylidene fluoride-*co*-trifluoroethylene-*co*-chlorotrifluoroethylene) [P(VDF-TrFE-CTFE)] random terpolymers films with different thermal annealing histories were studied in this work. First, the semicrystalline structure of the P(VDF-TrFE-CTFE) terpolymer films was studied by combined small-angle X-ray scattering and wide-angle X-ray diffraction analyses. A three-phase model was employed, namely, crystals, oriented and isotropic amorphous fractions (OAF and IAF). The bulky CTFE units generated taut-tie molecules (TTM) in the crystalline lamella, dividing it into many nanosized crystals (~1.3 nm thick). It is this unique crystalline structure with nanocrystals and mobile TTM/OAF that enabled the relaxor ferroelectric behavior for the P(VDF-TrFE)-based terpolymers. Through electrostriction measurements and nonlinear dielectric analysis, an inverse correlation was observed between the ferroelectric nonlinearity and the electrostrictive coefficient under a high poling electric field (>100 MV/m). This suggested that higher electrostriction performance could be achieved by decreasing the ferroelectric nonlinearity of the RFE terpolymer. Indeed, above the Curie temperature, the paraelectric terpolymer films achieved a high electrostrictive performance with the transverse strain being ~5% at 200 MV/m. This was attributed to the strong electrostatic repulsion among electric field-induced ferroelectric nanodomains. The finding from this work provides a viable way to design new electrostrictive polymers with higher performance at low driving fields.

Keywords: Electrostriction, poly(vinylidene fluoride-*co*-trifluoroethylene-*co*-chlorotrifloroethylene) random terpolymer, relaxor ferroelectric behavior, nanodomains, ferroelectric nonlinearity

Introduction

Under an external electric field, electrostrictive strain, which is proportional to the square of the induced polarization, can be generated in all dielectric materials.[1-2] Compared with the counterpart in ceramics,[2] electrostrictive polymers are featured by light weight, easy processing, and large electrostrictive strain, which are attractive for potential applications such as actuation,[1, 3-4] mechanical sensors,[5-6] and energy harvesting[7-9] in soft robotics. Due to the low dielectric constants (ε_r < 12) of most dielectric and ferroelectric polymers, the electrostrictive strain and electromechanical coupling factor are quite small. Intriguingly, a large electrostrictive strain (>4%) can be achieved for relaxor ferroelectric (RFE) polymers,[1, 4] such as electron beam-irradiated poly(vinylidene fluoride-*co*-trifluoroethylene) [P(VDF-TrFE)] random copolymers[4, 10] and P(VDF-TrFE-X) random terpolymers [X is either 1,1-chlorofluoroethylene (CFE) or chlorotrifluoroethylene (CTFE)].[11-12] Nonetheless, the fundamental electrostriction mechanism is still unclear. Previous studies have simply attributed the large electrostrictive strain in these RFE polymers to their high dielectric constant (ε_r > 40).[1]

Recently, our study has revealed the physical origin of negative Q_{33}/positive Q_{31} in PVDF-based ferroelectric polymers,[13] which has puzzled the field for quite a while.[14-15] Namely, different from ferroelectric ceramics, the conformational transformation of polymer chains in both crystals and the oriented amorphous fraction (OAF) makes the sample elongate along the transverse (i.e., 1) direction and shrink in the longitudinal (i.e., 3) direction. However, the nonlinear ferroelectric flipping with a large hysteresis should not be considered as genuine electrostriction. Two mechanisms of electrostriction in PVDF-based ferroelectric polymers are unraveled. The first is the mechano-electrostriction, which is caused by the electric field-induced conformational transformations between the twisted and zigzag chain conformations.[16] For normal ferroelectric

polymers with large ferroelectric domains, only dipoles in the OAF can respond to the applied electric field by chain conformational transformation when the electric field is below the coercive field (E_c). For RFE polymers, nanodomains can easily switch via chain conformational transformation, even under a low electric filed. Due to the low hysteresis of nanodomains switching, this conformational transformation is genuine mechano-electrostriction. The second mechanism is the electrostatic repulsion among highly polarized/aligned ferroelectric nanodomains in the transverse direction under a high electric field. In this sense, mechano-electrostriction is dominant under a low electric field, whereas electrostatic repulsion is dominant under a high electric field. Under a low electric field, the electrostriction coefficient Q_{31} is found to be inversely proportional to the product of Young's modulus and dielectric constant.[13, 17]

Although the understanding of mechano-electrostriction under a low electric field has been achieved in the previous study,[13] the mechanism of the electrostatic repulsion among ferroelectric nanodomains under high electric fields is still unclear. As we reported recently,[18] ferroelectric domains could be induced in the OAF under a high poling electric field. Therefore, the electrostatic repulsion between intrinsic ferroelectric nanodomains in crystal and electric field-induced nanodomains in OAF should be considered and investigated. In this work, four P(VDF-TrFE-CTFE) samples were prepared with different thermal annealing histories in the paraelectric phase. Their complex semicrystalline structures and electrostriction were studied to unravel the crystalline structure-electrostrictive property relationship.

Experimental Section

Materials. The P(VDF-TrFE-CTFE) random terpolymer with a molar ratio of 62.2/30.2/7.6 was kindly supplied by Piezotech/Arkema, Lyon, France. The number-average

molecular weight was determined by size-exclusion chromatography to be 276,000 g/mol and the dispersity index was 2.54, using linear polystyrene as the standard.[19] Polymer powders were used as received without further purification.

Films Fabrication and Processing. Four types of film samples were fabricated in this study. (1) *A quenched and stretched (terP-QS) sample.* Using nonsticking aluminum foils, the terpolymer was hot-pressed at 160 °C for 5 min at 6 tons, followed by quenching into liquid nitrogen. The quenched film was uniaxially stretched to an extension ratio of ca. 500% using a home-built stretching apparatus at room temperature. The stretching rate was 12 mm/min. This stretching condition remained the same for all samples in this study. (2) *A quenched, stretched, and 60 °C-annealed (terP-QSA60C) sample.* The QS sample was annealed at 60 °C for 12 h using an Instec HCS402 hot stage (Instec, Inc., Boulder, CO). (3) *A quenched, stretched, and 80 °C-annealed (terP-QSA80C) sample.* The QS sample was annealed at 80 °C for 12 h. (4) *A quenched, stretched, and 90 °C-annealed (terP-QSA90C) sample.* The QS sample was annealed at 90 °C for 48 h. Because the terP-QS sample annealed at 90 °C for 12 h behaved quite similar to the terP-QSA80C film, we prolonged the annealing time to 48 h. The final thicknesses of all films were around 20-35 μm.

Characterization and Instrumentation. Differential scanning calorimetry (DSC) experiments were carried out on a TA DSC250 (TA Instruments, New Castle, DE). Approximately 2 mg samples were used at a scanning rate of 10 °C/min under a dry nitrogen atmosphere (flow rate of 50 mL/min). Fourier transform infrared (FTIR) spectroscopy was performed on Thermo Scientific Nicolet iS50 (Thermo Fisher Scientific, Waltham, MA) and Agilent Cary 630 (Agilent Technologies, Santa Clara, CA) FTIR spectrometers. The scan resolution was 4 cm^{-1} with 32 scans. Broadband dielectric spectroscopy (BDS) measurements were carried out using a Novocontrol

Concept 80 broadband dielectric spectrometer (Novocontrol Technologies, Montabaur, Germany) with temperature control. The applied voltage was 1.0 V_{rms} (i.e., the root-mean-square voltage) with frequency ranging from 1 to 10^6 Hz and temperature from -50 to 100 °C. Gold (Au) electrodes with an area of 7.06 mm^2 were evaporated on both surfaces of samples using a Quorum Q300T D Plus sputter coater (Quorum Technologies, Ltd., Laughton, East Sussex, UK). The Au electrode thickness was 10 nm.

Two-dimensional (2D) small-angle X-ray scattering (SAXS) and wide-angle X-ray diffraction (WAXD) experiments were performed at the 11-BM Complex Material Scattering Beamline of the National Synchrotron Light Source II (NSLS-II), Brookhaven National Laboratory (BNL). The wavelength (λ) of the incident X-ray was 0.0729 nm. The distances between the sample and the WAXD (Pilatus 800 K, Dectris, Gaden-Dattwil, Switzerland) and the SAXS detectors (Pilatus 2M) were 261 and 5050 mm, respectively. These distances were calibrated using silver behenate with the first-order reflection at a scattering vector of $q = (4\pi\sin\theta)/\lambda = 1.076$ nm^{-1} (θ is the half scattering angle). The typical data acquisition time was 30 s.

Simultaneous electric displacement-electric field (D-E) and transverse strain-electric field (S_1-E) loops were measured using a Premiere II ferroelectric tester (Radiant Technologies, Inc., Albuquerque, NM) with a Trek 10/10B-HS high-voltage amplifier (0-10 kV AC, Trek, Inc., Lockport, NY), as described in previous reports.[20-21] The applied voltage had a bipolar sinusoidal waveform at 1 Hz. The film samples were coated with gold (Au) electrodes on both sides with an overlapping area of 8×3 mm^2. The Au-coated film was immersed in silicone oil to avoid corona discharge in air. The stray capacitance was determined using a biaxially oriented polypropylene film (8 μm, provided by SB Electronics, Inc., Barre, VT) with a dielectric constant of 2.25. The

S_1 of the film samples (the initial length = 8 mm) was measured using a home-built fixture connected to a MTI 2100 fotonic sensor (MTI Instruments, Inc., Albany, NY), following a previous report.[21] At high temperatures (>35 °C), significant conduction was observed in D-E loops in the large-area terpolymer films. To overcome this problem, separate D-E loop measurements were performed on small-area samples (7.06 mm^2). A home-built sample fixture was used to connect the Au electrodes on both sides of the film with the interface of the Radiant ferroelectric tester using high-voltage cables. The temperature was controlled using a ChemGlass CG-1999-V-10 hot plate (ChemGlass Life Sciences, LLC, Vineland, NJ).

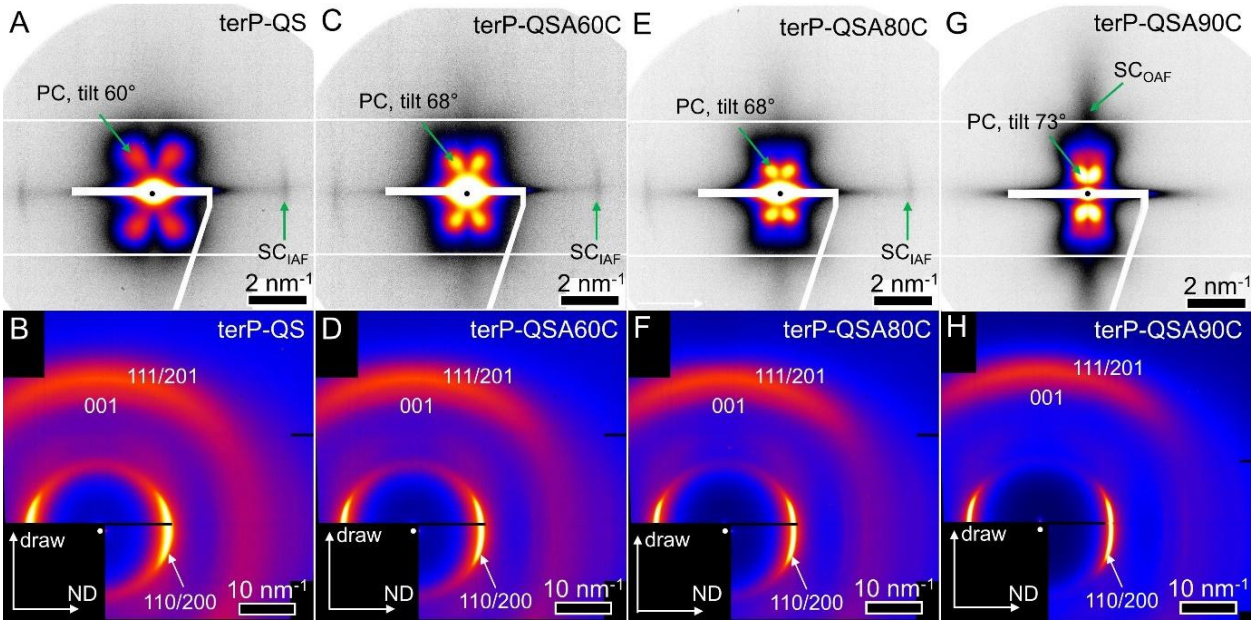

Figure 1. Two-dimensional (2D) (A,C,E,G) SAXS and (B,D,F,H) WAXD patterns for (A,B) terP-QS, (C,D) terP-QSA60C, (E,F) terP-QSA80C, and (G,H) terP-QSA90C films at room temperature. The drawing is along the vertical direction and the film normal direction (ND) is along the horizontal direction.

Result and Discussion

Unique Semicrystalline Structure with Nanosized Ferroelectric Domains in the P(VDF-TrFE-CTFE) Terpolymers. In the past, a two-phase model was used to describe the

RFE terpolymers, i.e., crystals and the amorphous phase. Due to the repeat-unit isomorphism, it was considered that bulky CTFE units were included in the crystals.[11, 19] However, on the basis of our recent reports on PVDF-based homopolymers and random copolymers, this two-phase model cannot fully describe their complicated crystalline structures. Instead, a three-phase model should be employed, namely, crystal, the oriented and isotropic amorphous fractions (OAF and IAF).[18, 22] Therefore, the semicrystalline structure of the P(VDF-TrFE-CTFE) random terpolymers needs to be revisited.

Figures 1A,C,E,G show 2D SAXS patterns for different terpolymer samples. Butterfly-like primary crystal (PC) scattering patterns were observed for all samples, indicating that the crystalline lamellae were tilted at an angle (60-73°) from the stretching direction. Upon increasing the annealing temperature, the butterfly scattering peaks gradually approached the beam center, indicating an increased lamellar spacing due to lamellar thickening via chain-sliding in the paraelectric phase. In addition, a weak scattering peak with a *d*-spacing of 4.1 nm was seen on the equator, which was attributed to the lamellar stacking of secondary crystals in the IAF, as we reported before.[23] The 2D WAXD patterns of different terpolymer samples are shown in Figures 1B,D,F,H, respectively. A sharp (110/200) reflection (K_1) was seen on the equator, and extremely broad (001/111/201) reflections (K_2) were observed on the meridian.

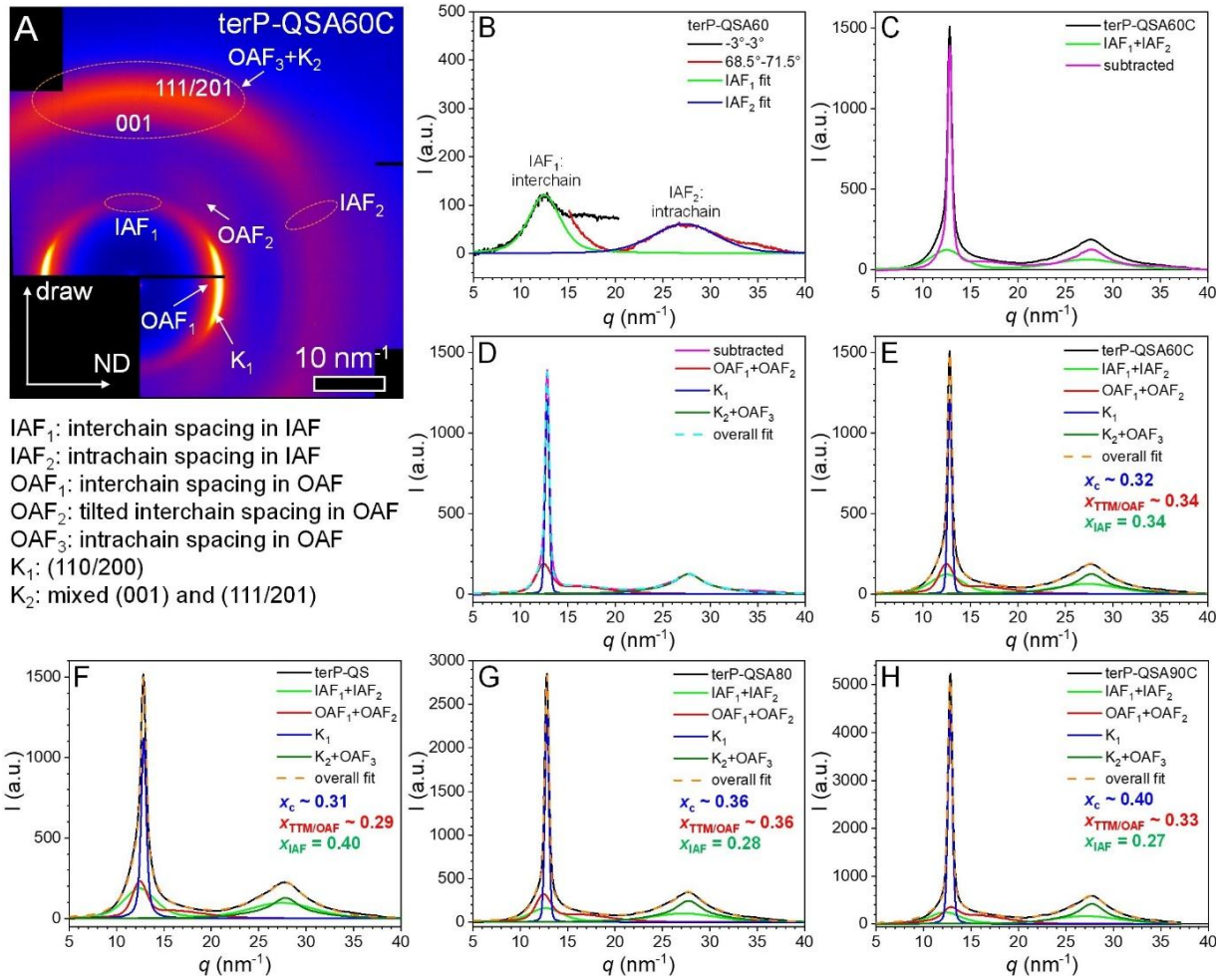

Figure 2. (A) 2D edge-on WAXD pattern of the terP-QSA60C film at room temperature. The drawing direction is vertical, and the film ND is horizontal. Different scatterings and diffractions are indicated in the WAXD pattern. (B) Fitted IAF_1 [from the integrated region of -3° - 3° in (A)] and IAF_2 scatterings [from the integrated region of 68.5° - 71.5° in (A)]. The Guassian+Lorentzian functions are used for peak-fitting. (C) The subtracted WAXD curve (magenta) for crystal diffractions and OAF scatterings after the sample intensity (black) subtracts the total IAF (IAF_1+IAF_2) scattering (green). (D) Fitting of the subtracted WAXD curve in (C), using OAF_1+OAF_2 scattering (red), K_1 diffraction (blue), and K_2+OAF_3 scattering (olive). (E) The final fitting result of the terP-QSA60C WAXD curve using total IAF scattering (green), OAF_1+OAF_2 scattering (red), K_1 diffraction (blue), and K_2+OAF_3 scattering (olive). The final fitting results are presented in (F) terP-QS, (G) terP-QSA80C, and (H) terP-QSA90C.

Figure 2A shows the 2D edge-on WAXD pattern of the terP-QSA60C sample. Three oriented halo-scatterings around the PC (i.e., K_1 and K_2) reflections were observed, which could be assigned to the OAF scatterings, including OAF_1 around K_1, OAF_2 (a weak scattering extending from K_1 to K_2), and OAF_3 around K_2. Meanwhile, two IAF scatterings could be seen in the areas

free of the crystalline reflections, namely, IAF_1 at ~12 nm^{-1} on the meridian and IAF_2 at 27 nm^{-1} in the quadrant. They could be ascribed to the average interchain (~0.5 nm) and intrachain (or inter-bond, ~0.23 nm) spacing in the IAF, respectively. A schematic representation of the three-phase morphology is shown in Scheme 1A, where chain-folding is not the major structure at the crystal-amorphous interfaces. Instead, many chains extend out of the crystals, forming the OAF. The orientation of chains gradually tapers off from the crystal basal planes and finally IAF is formed in the middle of the amorphous layer. In this sense, the OAF is more liquid crystal-like, rather than amorphous. Because the OAF chains stem out from the crystal basal planes, lamellar tilting is resulted to reduce chain-crowding at the crystal-amorphous interfaces. Usually, OAF has a lower mobility than IAF due to its direct tethering of at least one end to the rigid crystals. If a significant portion of OAF vitrifies, it becomes the so-called rigid amorphous fraction (RAF).[24-25]

The overall lamellar spacings of all the terpolymer samples were calculated from one-dimensional (1D) correlation function analysis using the SasView software (for details see Figure S1). As shown in Figure 3A, the lamellar spacing increased from 12.6 nm for terP-QS to 27.2 nm for terP-QSA90C (i.e., an extended-chain crystalline morphology), as a result of lamellar thickening due to thermal annealing in the paraelectric phase.[26-28] Assuming a crystallinity of ~0.3, the crystalline layer was estimated to be ~3.8 nm for terP-QS. However, from the Scherrer analysis, the crystallite size for (001/111/201) ($\tau_{//}$) was estimated to be ~1.3 nm (see Figure 3B), indicating that the crystalline correlation was extremely small along the chain axes. Therefore, a lot of conformational defects (e.g., kinks and twists) caused by the bulky CTFE unit must exist in the crystalline layer, forming taut-tie molecules (TTM) between neighboring crystals. Note that the kink band in the cooled phase of P(VDF-TrFE), as proposed by Tashiro, contains a layer of single trans-to-gauche twisted conformation.[29-30] It is possible that the bulky CTFE units caused more

twists in the crystalline region. Combining both SAXS and WAXD analyses, the semicrystalline structure of the P(VDF-TrFE-CTFE) terpolymer can be explained in Scheme 1B. The crystalline layer contains alternating thin crystal (~1.3 nm) and finite TTM layer with conformational twists, and the amorphous layer contains both OAF and IAF. In the IAF, certain secondary crystals (SC_{IAF}) could grow (represented as the dashed rectangles in Scheme 1B), which gave the weak scattering on the equator of the SAXS patterns (Figures 1A,C,E). This unique semicrystalline structure is believed to be the origin of RFE behavior reported before.[1, 4, 11]

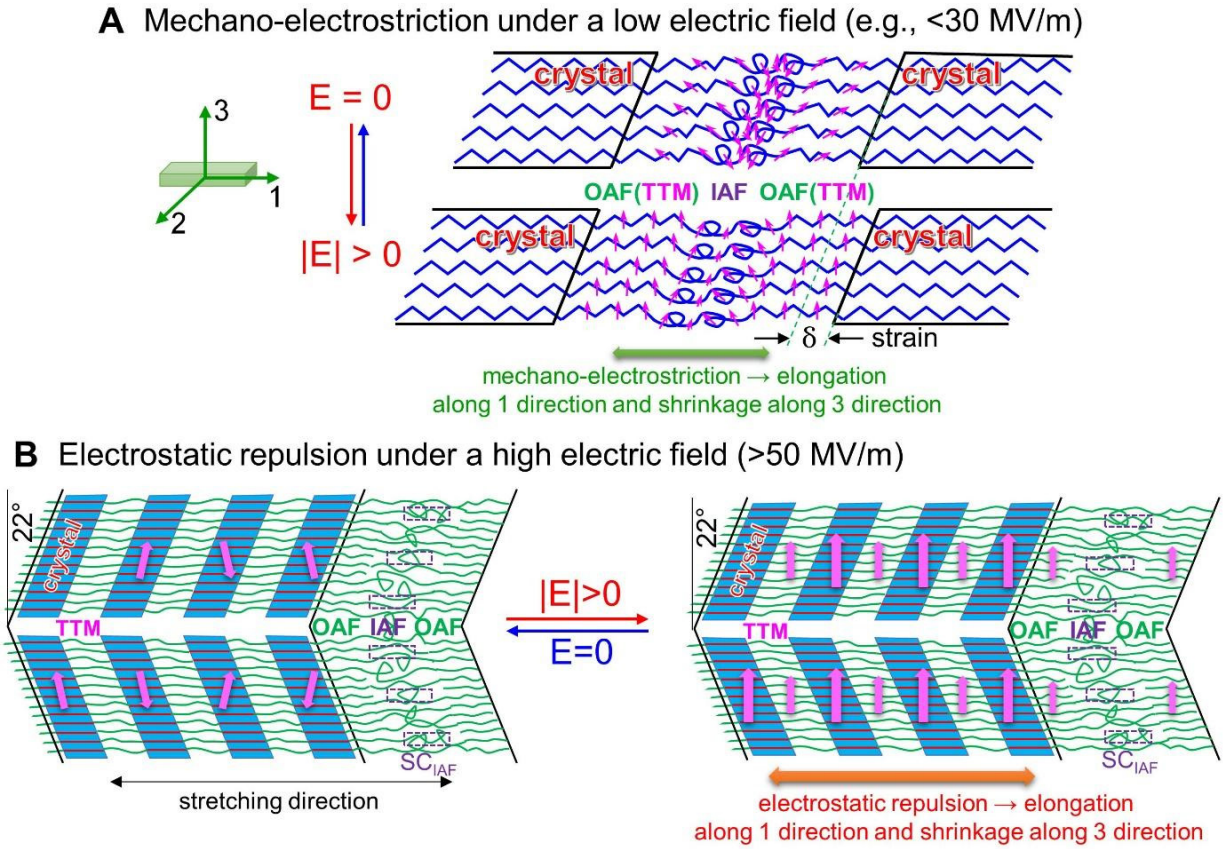

Scheme 1. Schematic representations of (A) mechano-electrostriction due to the twisted-to-zigzag conformation transformation in OAF or TTM under a low electric field (e.g., < 30MV/m) and (B) electrostatic repulsion among polarized nanodomains in crystals, TTM, and OAF under a high electric field (e.g., > 50 MV/m).

According to our recent reports,[13, 23] the contents of PCs (x_c), TTM/OAF ($x_{TTM/OAF}$; note

that the structures of TTM and OAF are similar and it is not possible to differentiate them in the WAXD pattern), and IAF (x_{IAF}) could be determined using quantitative 2D WAXD analysis. As shown in Figure 2B, the IAF_1 and IAF_2 scatterings could be obtained by integrating regions I (-3°-3° up to 20 nm^{-1}) and II (68.5°-71.5° from 17 to 39 nm^{-1}), respectively. After subtracting the total IAF (i.e., IAF_1+IAF_2) scattering from the overall 1D WAXD curve, a subtracted curve was obtained (Figure 2C). This subtracted WAXD curve was further deconvoluted into OAF_1+OAF_2 scattering (red), K_1 diffraction (blue), and K_2+OAF_3 scattering (olive) using the PeakFit software (Systat Software, Inc.) (Figure 2D). However, due to the extremely broad (001/111/201) reflections, it was not possible to differentiate the K_2 diffraction from the OAF_3 scattering in the WAXD pattern. If we assume that the ratio of OAF_3 to K_2 was 1:1, then x_c, $x_{TTM/OAF}$, and x_{IAF} could be estimated from the integrated peaks for terP-QSA60C in Figure 2E. Similarly, the final fitting results and the estimated x_c, $x_{TTM/OAF}$, and x_{IAF} values for terP-QS, terP-QSA80C, and terP-QSA90C are shown in Figures 2F,G,H, respectively.

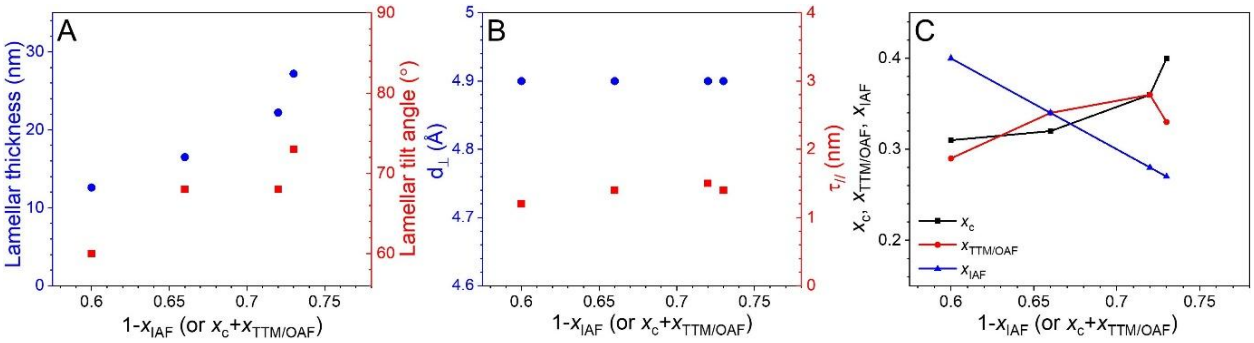

Figure 3. (A) Lamellar thickness and tilt angle, (B) *d*-spacing of the (110/200) reflection ($d_\perp$) and the crystallite size of (001/111/201) reflection ($\tau_{//}$), and (C) x_c, $x_{TTM/OAF}$, and x_{IAF} as a function of 1-x_{IAF} or x_c+$x_{TTM/OAF}$ for various P(VDF-TrFE-CTFE) terpolymer films.

The above estimation allowed us to understand the thermal annealing effect on the semicrystalline morphology of different terpolymer samples. Figure 3C shows the x_c, $x_{TTM/OAF}$,

and x_{IAF} as a function of 1-x_{IAF} or x_c+$x_{TTM/OAF}$. Upon thermal annealing terP-QS at an increasingly higher temperature, x_{IAF} decreases linearly with respect to x_c+$x_{TTM/OAF}$. Meanwhile, x_c increased, and $x_{TTM/OAF}$ first increased up to 80 °C and finally slightly decreased upon annealing at 90 °C for 48 h. Because the structures of TTM and OAF were fairly similar, it was not possible to further differentiate them using the WAXD analysis. From this result, we understand that thermal annealing in the paraelectric phase increased the content of oriented structures (both crystals and TTM/OAF) in the terpolymer, at the expense of decreasing x_{IAF}. FTIR was used to study the local chain conformation in different samples. As shown in Figure S2, no obvious difference was observed, indicating that the local chain conformations of the terpolymer films annealed at different temperatures were similar.

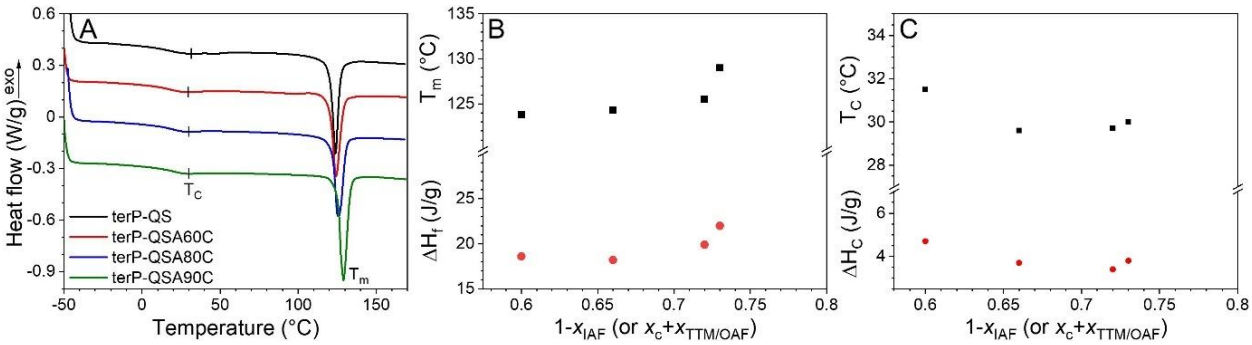

Figure 4. (A) The first heating DSC curves for various P(VDF-TrFE-CTFE) films. The heating rate is 10 °C/min. (B) Melting point (T_m) and melting enthalpy (ΔH_f) and (C) Curie temperature (T_C) and heat of Curie transition (ΔH_C) as a function of 1-x_{IAF} or x_c+$x_{TTM/OAF}$ of the terpolymer films.

The first heating DSC curves of all the terpolymer samples are shown in Figure 4A. In addition to the melting temperature (T_m) around 125 °C, a broad Curie transition around 30 °C was observed. Upon increasing the annealing temperature, the T_m gradually increased from 123.8 °C for terP-QS to 129 °C terP-QSA90C, indicating crystalline lamellar thickening (Figure 4B). This is consistent with the SAXS/WAXD results above. After annealing at 90 °C for 48 h, the terP-

QSA90C achieved more or less extended-chain crystalline morphology. The melting enthalpy (ΔH_f) reached 22.0 J/g (Figure 4B), which is considered to have contributions from both crystals and liquid crystal-like TTM/OAF; therefore, it is not possible to calculate the heat of fusion for perfect extended-chain terpolymer crystals. For the thermally annealed samples, terP-QSA90C exhibited higher Curie temperature (T_C) and Curie transition (ΔH_C), suggesting that extensive thermal annealing could grow larger crystals and thus larger ferroelectric domains.

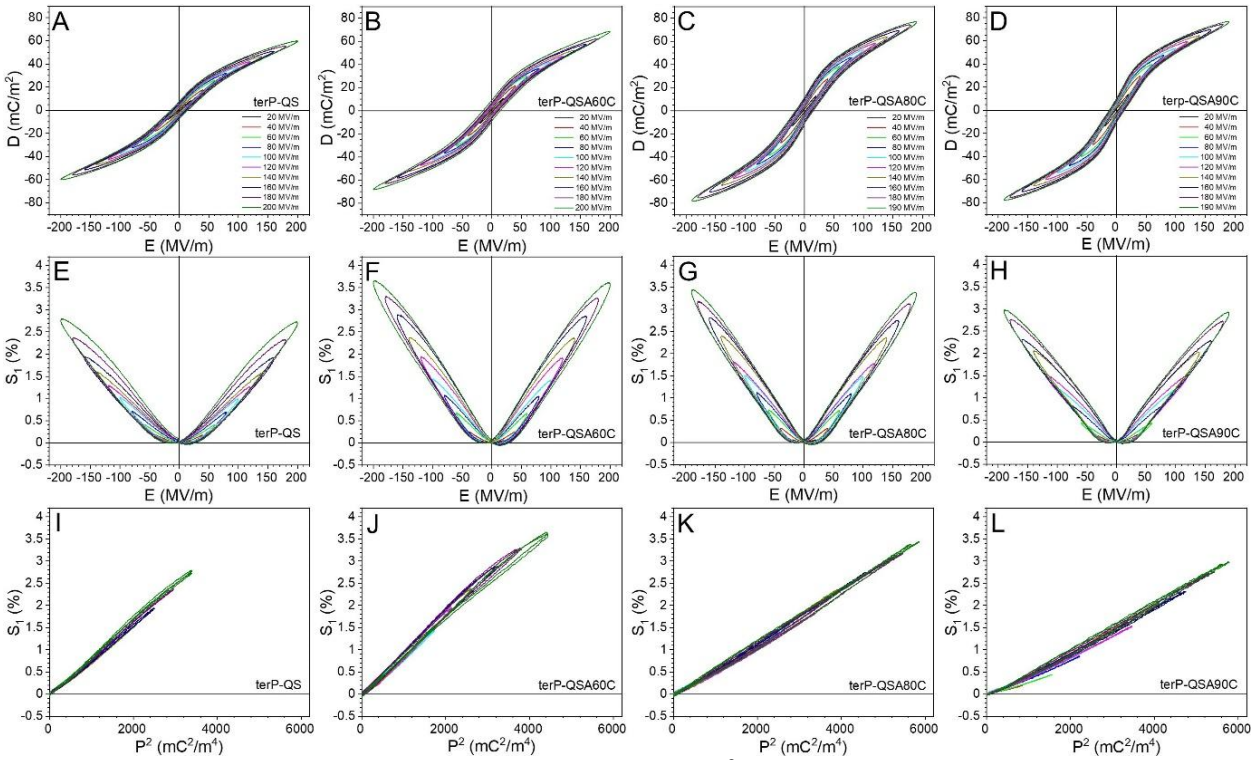

Figure 5. Bipolar (A-D) D-E, (E-H) S_1-E, and (I-L) S_1-P^2 loops for different P(VDF-TrFE-CTFE) films at room temperature under different poling fields: (A,E,I) terP-QS, (B,F,J) terP-QSA60C, (C,G,K) terP-QSA80C, and (D,H,L) terP-QSA90C. The poling frequency is 1 Hz with a sinusoidal waveform.

Electrostrictive Performance of P(VDF-TrFE-CTFE) Films at Room Temperature. As we discussed above, thermal annealing in the paraelectric phase decreased x_{IAF} and increased x_c and $x_{TTM/OAF}$ for P(VDF-TrFE-CTFE). What would be the effect of x_c and $x_{TTM/OAF}$ on the

electrostrictive performance? To answer this question, we measured simultaneous D-E and S_1-E loops for different terpolymer samples at room temperature under different poling electric fields (Figures 5A-H). In order to avoid the transient response and the remanent S_1 during the first loops, the second D-E and S_1-E loops were presented in this study.[13]

As shown in Figures 5A-D, the D-E loops became increasingly broader with increasing the annealing temperature, indicating enhanced ferroelectricity after annealing. Meanwhile, the maximum D also increased. Figure 6A presents the D values of different terpolymer samples as a function of the poling electric field. The terP-QS exhibited the lowest D under all electric fields, and the D of terP-QSA60C was higher. From the above WAXD analysis (Figure 3C), the increase in D should be attributed to the decreased x_{IAF} after thermal annealing. Since the x_c values of terP-QS and terP-QSA60C samples were almost the same, the enhancement of D for terP-QSA60C should be ascribed to its increased $x_{TTM/OAF}$. Finally, terP-QSA80C and terP-QSA90C had the highest D and their D curves almost overlapped. This could be attributed to the significantly increased x_c for both samples (Figure 3C). The higher $x_{TTM/OAF}$ and x_c would increase the ferroelectric domain size upon high-field electric poling. Therefore, the increased D was a result of increase ferroelectric domain size for the terpolymer samples upon increasing the annealing temperature. The question is: will the higher D enhance electrostriction?

The electrostrictive performance is shown in Figures 5E-H, and parabolic-like S_1-E loops were observed, which is typical for RFE polymers.[1, 4, 13] Figure 6B summarizes the maximum S_1 as a function of the poling electric field for different terpolymer samples. When the poling field was below 30 MV/m, the S_1 difference for various terpolymer samples was quite small. It became more obvious when the poling field was above 50 MV/m. From Figure 6B, S_1 was the lowest for terP-QS. It reached the maximum values for terP-QSA60C and terP-QSA80C, and then decreased

for terP-QSA90C. Therefore, a higher D did not necessarily guarantee a higher electrostrictive performance.

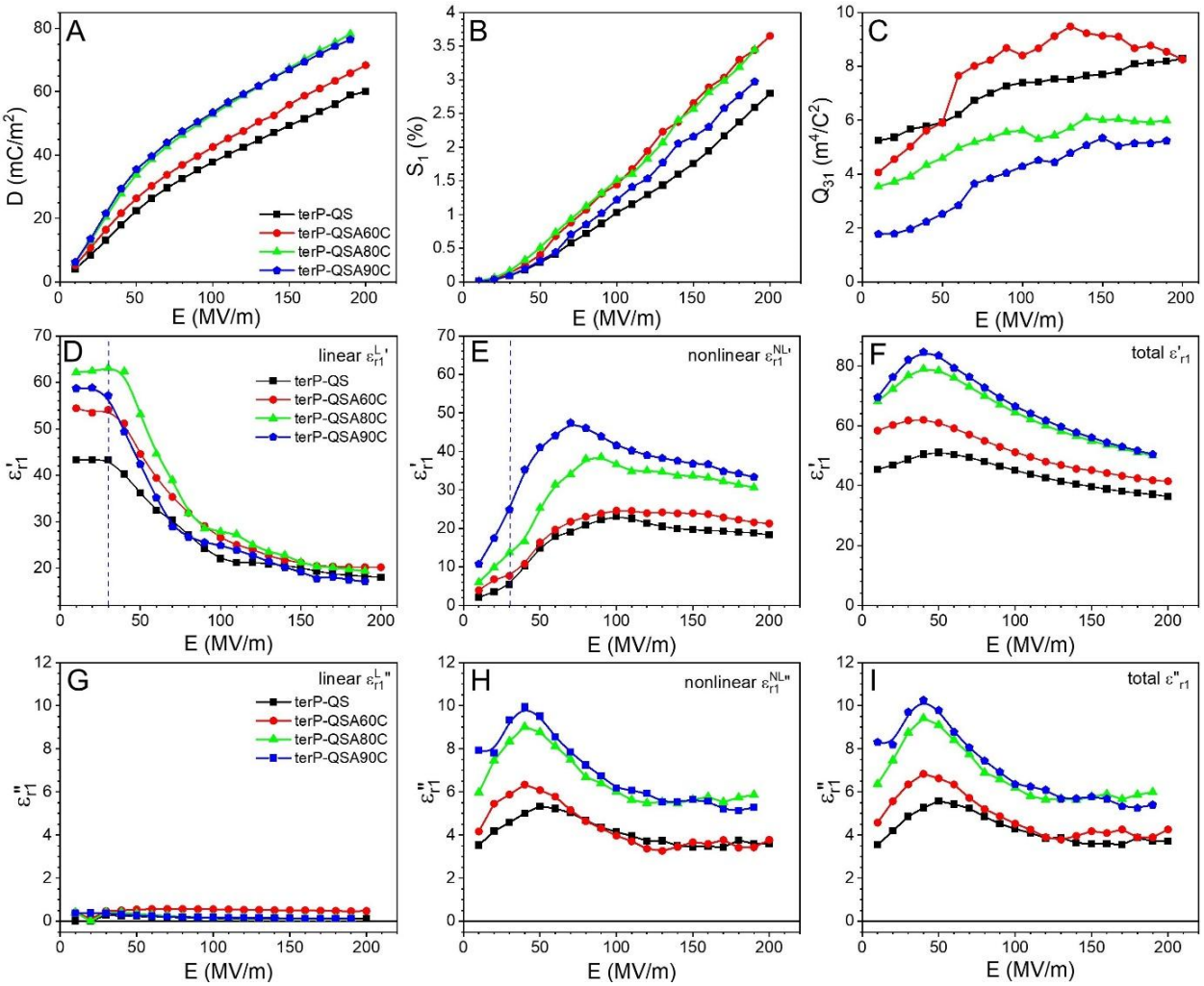

Figure 6. Maximum (A) D and (B) S_1, and (C) calculated Q_{31} as a function of the poling electric field for different P(VDF-TrFE-CTFE) films at room temperature. (D,G) Linear $\varepsilon_{r1}^{L\prime}$ and $\varepsilon_{r1}^{L\prime\prime}$, (E,H) nonlinear $\varepsilon_{r1}^{NL\prime}$ and $\varepsilon_{r1}^{NL\prime\prime}$ and (F,I) overall $\varepsilon_{r1}^{\prime}$ and $\varepsilon_{r1}^{\prime\prime}$ as a function of the poling electric field for different P(VDF-TrFE-CTFE) films at room temperature.

The other important factor for electrostriction is the electrostrictive coefficient, Q_{31}. Because $S_1 = Q_{31}P^2$ for RFE polymers, Q_{31}, could be obtained from the linear region in the S_1-P^2 loops (Figures 5I-L). Figures 6C summarizes the Q_{31} of different terpolymer samples as a function of the poling electric field. All terpolymer samples showed a similar trend, namely, Q_{31} firstly

increased with the electric field for E < 50 MV/m, and the increase became smaller or Q_{31} leveled off above 90 MV/m. When the poling field was above 50 MV/m, the Q_{31} of the terP-QSA60C reached the highest values and then decreased with further increasing the annealing temperature.

There is a question: What is the working mechanism behind the Q_{31} of different terpolymer samples? As shown in Scheme 1A, mechano-electrostriction is dominant under a low electric field (e.g., <30 MV/m), which originates from electric field-induced twisted-to-zigzag conformational transformation in the nanocrystals and TTM/OAF, as reported before.[13] From Figure 6B, the difference of mechano-electrostriction between different terpolymer samples was small. When the external field is zero, ferroelectric nanodomains exist only in the crystals, not in the TTM and OAF (see the left panel of Scheme 1B). Above 50 MV/m, additional ferroelectric nanodomains could be induced in the TTM and OAF by the high poling field. Because all these aligned nanodomains are closely packed, the electrostatic repulsion among them significantly enhances electrostriction (see the right panel of Scheme 1B). After the external field is removed, the electric field-induced nanodomains in TTM/OAF should largely disappear. Therefore, the high-field electrostriction in Figure 6C should primarily originate from the electrostatic repulsion among existing (in crystals) and field-induced (in TTM and OAF) nanodomains.

To understand different Q_{31} values in different terpolymer films, nonlinear dielectric analysis was performed,[13, 18, 31-32] and the procedure is presented in Scheme S1. Here, we use the terP-QS as an example. Following our previous reports,[13, 18, 31] the linear deformational polarization (D_{def}), which originates from electronic and atomic polarizations of the entire sample and the orientational polarization from the amorphous phase, was first determined. After subtracting the linear D_{def} from the D-E loops in Figure 5A, the nonlinear polarization (P_{NL})-E loops for the terP-QS were obtained, as shown in Figure S3A. Then, the overall D(t), the linear

$D_L(t)$, and the nonlinear $P_{NL}(t)$ waves were plotted in Figures S3B-D, respectively. After applying Fourier transform for the overall D(t), linear $D_L(t)$, and nonlinear $P_{NL}(t)$ waves, the complex overall D_n^* (n=1,2,3,4,5, etc.), linear D_1^{L*}, and nonlinear D_n^{NL*} were obtained. Then, the complex overall ε_{rn}^*, linear ε_{r1}^{L*}, and nonlinear ε_{rn}^{NL*} were determined using the equation, $\varepsilon_{rn}^*(\varepsilon_{r1}^{L*}, \varepsilon_{rn}^{NL*}) = D_n^*(D_1^{L*}, D_n^{NL*})/(\varepsilon_0 E)$, where ε_0 is vacuum permittivity and E is electric field: ε_{r1}' (linear, nonlinear, total) in Figure S3E, ε_{r1}'' (linear, nonlinear, and total) in Figure S3F, $\varepsilon_{r3}^{NL\prime}$ and $\varepsilon_{r3}^{NL\prime\prime}$ in Figure S3G, and $\varepsilon_{r5}^{NL\prime}$ and $\varepsilon_{r5}^{NL\prime\prime}$ in Figure S3H. This nonlinear dielectric analysis was also performed for the D-E loops of terP-QSA60C, terP-QSA80C, and terP-QSA90C in Figures 5B-D, and the results are shown in Figures S4-S6, respectively. Compared with the first harmonics, the higher order harmonics were small, and we can focus on the first harmonics for discussion.

Figures 6D-I summarize the complex first harmonics as a function of the electric field for different terpolymer films. Below 30 MV/m, linear $\varepsilon_{r1}^{L\prime}$ remained constant for all samples; 43.5 for terP-QS, 53.9 for terP-QSA60C, 62.6 for terP-QSA80C, and 57.9 for terP-QSA90C (Figure 6D). These values are consistent with the BDS results in Figure S7. When the electric field was above 30 MV/m, linear $\varepsilon_{r1}^{L\prime}$ quickly decreased and leveled off around 19.5 above 150 MV/m for all films. From Figures 6E,H the nonlinear $\varepsilon_{r1}^{NL\prime}$ and $\varepsilon_{r1}^{NL\prime\prime}$ of terP-QS and terP-QSA60C were similar and much lower than those of terP-QSA80C and terP-QSA90C. Compared with the Q_{31} in Figure 6C, the terP-QS and terP-QSA60C samples with a lower nonlinear $\varepsilon_{r1}^{NL\prime}$ had a higher Q_{31}, and the terP-QSA90C with the highest nonlinear $\varepsilon_{r1}^{NL\prime}$ had the lowest Q_{31}. This inverse correlation suggests that the dielectric nonlinearity is detrimental to Q_{31}. In other words, ferroelectric nonlinearity from larger crystals in heavily annealed terpolymers should be avoided for high electrostriction performance. This is consistent with our recent study comparing P(VDF-TrFE) 75/25 (mol./mol.) and P(VDF-TrFE-CTFE) terpolymer,[13] where the ferroelectric P(VDF-TrFE)

75/25 exhibited a much smaller electrostrictive strain than the RFE terpolymer.

Finally, according to the above electrostriction equation, the overall electrostrictive strain has a combined contribution from D and Q_{31} (Figure 6B). For terP-QSA60C, Q_{31} is the highest but D is somewhat lower. For terP-QSA80C, D is the highest but Q_{31} is lower. As a result, their electrostrictive performance is similarly high. For terP-QS, D is the lowest and thus the electrostrictive performance is the lowest. For terP-QSA90C, the Q_{31} is the lowest and thus the electrostrictive performance is lower than that of terP-QSA60C and terP-QSA80C.

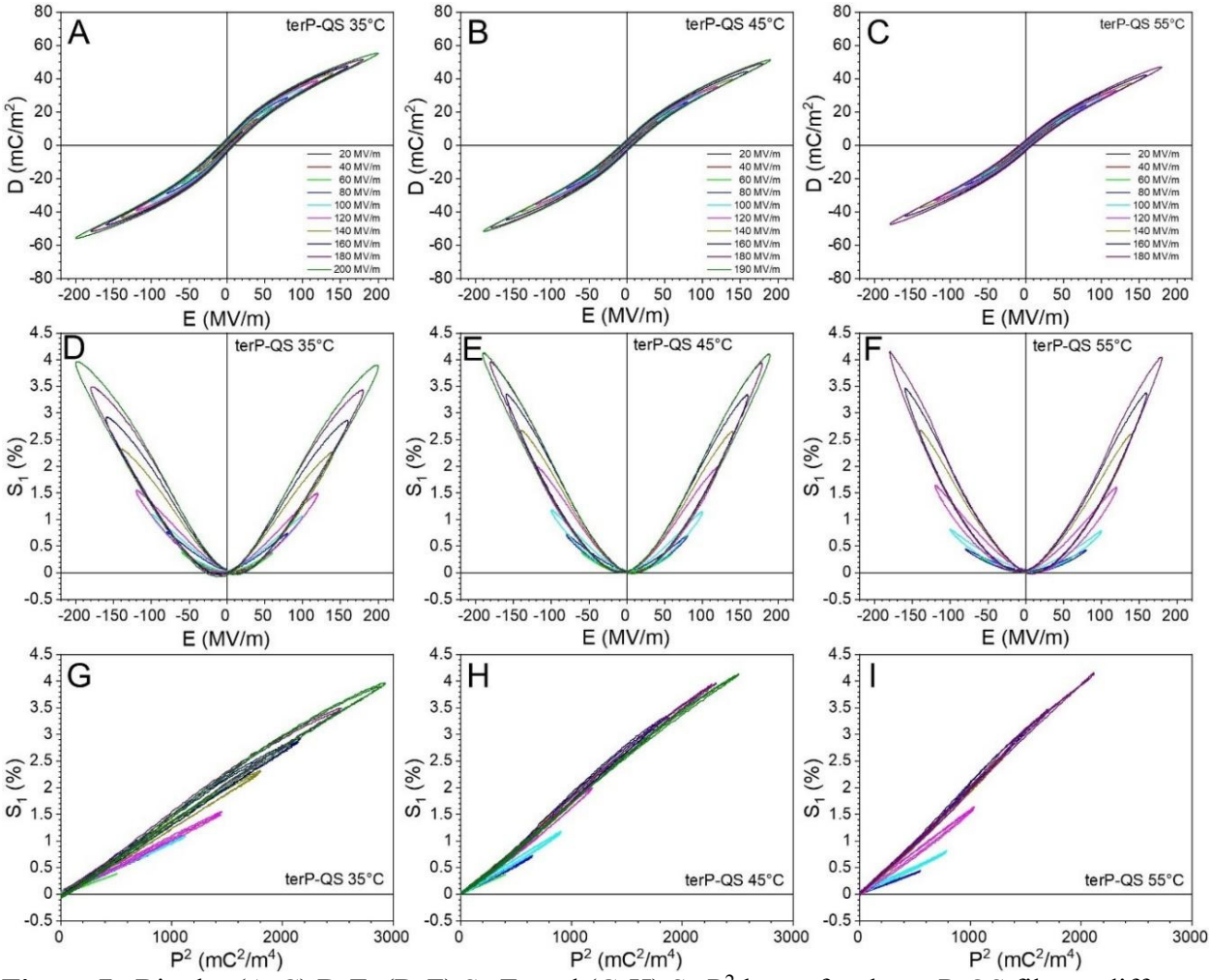

Figure 7. Bipolar (A-C) D-E, (D-F) S_1-E, and (G-H) S_1-P^2 loops for the terP-QS film at different temperatures under different poling electric fields: (A,D,G) 35 °C, (B,E,H) 45 °C, and (C,F,I) 55 °C. The poling frequency is 1 Hz with a sinusoidal waveform.

Further Enhancing Electrostriction at Elevated Temperatures. From the room temperature study, we consider that electrostriction could be further enhanced by decreasing the ferroelectric nonlinearity of the terpolymer films. To verify this idea, a simple and effective way is to increase the temperature above T_C and study electrostriction of the paraelectric terpolymer films. Figure 7 shows the electrostrictive performance of terP-QS at different temperatures. As shown in Figures 7A-C, the D-E loops above T_C were much slimmer than those at 25 °C (Figure 5A). This could be attributed to the much smaller field-induced ferroelectric nanodomains in the paraelectric phase, and thus decreased ferroelectric nonlinearity. Note that even in the paraelectric phase above T_C, a high enough electric field can still induce ferroelectric nanodomains.[33-35] Figure 8A presents the maximum D of terP-QS as a function of the poling electric field at different temperatures, and it decreased with increasing temperature. Parabolic shaped S_1-E loops for terP-QS sample were seen in Figures 7D-F, and they also became slimmer upon increasing temperature. Figures 8B summarizes S_1 as a function of the poling electric field at different temperatures. Below 100 MV/m, the S_1-E curves at 25, 35, and 45 °C overlapped; however, the S_1 at 55 °C was lower. This is because 55 °C was much higher than the T_C of terP-QS, and few field-induced ferroelectric nanodomains could be induced under such a low electric field. When the electric field was above 100 MV/m, S_1 of terP-QS was higher at higher temperatures. This is counterintuitive, because we had expected lower electrostriction performance when temperature was increasingly higher than T_C.

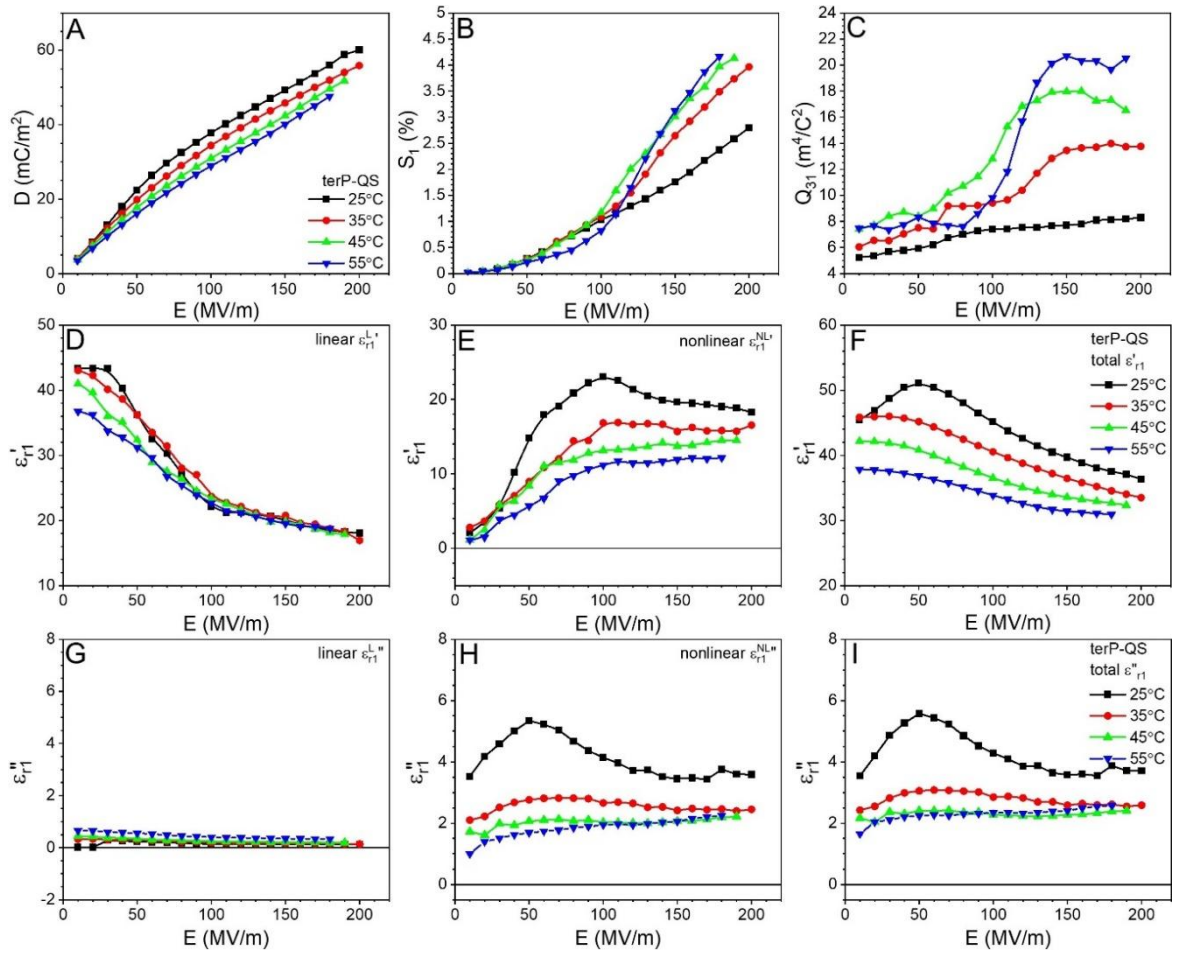

Figure 8. Maximum (A) D and (B) S_1, and (C) calculated Q_{31} as a function of the poling electric field for terP-QS at different temperatures. (D,G) Linear $\varepsilon_{r1}^{L\prime}$ and $\varepsilon_{r1}^{L\prime\prime}$, (E,H) nonlinear $\varepsilon_{r1}^{NL\prime}$ and $\varepsilon_{r1}^{NL\prime\prime}$ and (F,I) overall $\varepsilon_{r1}^{\prime}$ and $\varepsilon_{r1}^{\prime\prime}$ as a function of the poling electric field for the terP-QS film at different temperatures.

To explain this counterintuitive observation, we need to study Q_{31} and correlate it with the nonlinear dielectric property. From the S_1-P^2 loops in Figures 7G-I, Q_{31} as a function of electric field was obtained for terP-QS at different temperatures. Different from the Q_{31}-E curve at 25 °C, the Q_{31}-E curves of terP-QS at 35, 45, and 55 °C showed a similar trend. Namely, Q_{31} first increased slowly below 70 MV/m, increased sharply above 100 MV/m, and finally leveled off above 140 MV/m. This indicated that a high enough field was required to induce ferroelectric nanodomains in the paraelectric phase. The maximum Q_{31} increased with an increase of temperature: ~7.7 m^4/C^2 at 25 °C, ~13.8 m^4/C^2 at 35 °C, ~17.9 m^4/C^2 at 45 °C, and ~20.5 m^4/C^2 at

55 °C. Intriguingly, the maximum Q_{31} of terP-QS at 55 °C was nearly 2 times higher than that at 25 °C.

To understand this dramatic increase in Q_{31} above 100 MV/m at elevated temperatures, nonlinear dielectric analysis was performed on the D-E loops in Figures 7A-C, the results are displayed in Figures S8-S10, respectively. Figures 8D-I summarize the first harmonics vs. the poling electric field at different temperatures, and linear $\varepsilon_{r1}^{L\prime}$, nonlinear $\varepsilon_{r1}^{NL\prime}$, and overall $\varepsilon_{r1}^{\prime}$ of terP-QS at different temperatures are presented in Figures 8D,E,F, respectively. Above 100 MV/m, the linear $\varepsilon_{r1}^{L\prime}$ at different temperatures were almost the same. The nonlinear $\varepsilon_{r1}^{NL\prime}$ increased first and leveled off above 100 MV/m. The maximum $\varepsilon_{r1}^{NL\prime}$ value decreased with increasing temperature, indicating a decrease in ferroelectric nonlinearity with temperature. In other words, the poling field-induced ferroelectric nanodomains were smaller in size at elevated temperatures. Compared with the Q_{31} changes in Figure 8C, terP-QS with a lower nonlinear $\varepsilon_{r1}^{NL\prime}$ at 55 °C had the highest Q_{31} of 20.5 m^4/C^2. Again, an inverse correlation between the ferroelectric nonlinearity and Q_{31} was observed. Indeed, enhanced electrostrictive performance for terP-QS was achieved under a high enough poling field (>100 MV/m) at elevated temperatures due to the decreased ferroelectric nonlinearity in the paraelectric phase.

In addition to terP-QS, the high-temperature electrostriction performance was also studied for terP-QSA60C, as shown in Figure S11. The nonlinear dielectric analysis was performed for the D-E loops in Figure S11A-C, and results are presented in Figures S12-S14. The maximum D and S_1 under different poling fields are summarized in Figures S15A,B. When the poling field was above 100 MV/m, again increased S_1 was observed for terP-QSA60C at an increasingly higher temperature. From the S_1-P^2 loops in Figures S11G-I, Q_{31} was obtained in Figure S15C. Above 100 MV/m, Q_{31} values at 45 and 55 °C were higher than those at 25 and 35 °C. From nonlinear

dielectric analysis results (Figures S15D-I), the linear $\varepsilon_{r1}^{L\prime}$ values were similar for terP-QSA60C above 100 MV/m at all temperatures. However, the $\varepsilon_{r1}^{NL\prime}$ gradually decreased upon increasing temperature (Figure S15E). Again, an inverse correlation was observed between Q_{31} and $\varepsilon_{r1}^{NL\prime}$. Namely, terP-QSA60C at 45 and 55 °C had the lowest $\varepsilon_{r1}^{NL\prime}$ but the highest Q_{31}. Based on Q_{31} and D, the S_1 values reached the highest for 45 and 55 °C: ~4.9% at 200 MV/m. This value was about 36% higher than the S_1 at 25 °C (3.6%).

Conclusions

In summary, the semicrystalline structure of the P(VDF-TrFE-CTFE) terpolymer was revisited using combined SAXS and WAXD analyses. Instead of the conventional two-phase model, a three-phase model should be employed to describe the complex semicrystalline morphology, i.e., crystals, OAF, and IAF. Within the crystalline layer, alternating thin crystals (1.3 nm thick) and finite TTM layers were present. From the WAXD analysis, x_c, $x_{TTM/OAF}$, and x_{IAF} were determined. Upon increasing the thermal annealing temperature and time in the paraelectric phase, x_{IAF} decreased and $x_c/x_{TTM/OAF}$ increased. Finally, after annealing at 90 °C for 48 h, an extended-chain crystalline structure was obtained with larger crystals and intrinsic ferroelectric nanodomains.

Electrostriction performance of different terpolymer films was studied, and the structure-property relationship was unraveled. Two mechanisms of electrostriction were identified: mechano-electrostriction due to conformational transformation at low fields (e.g., < 30 MV/m) and electrostatic repulsion among field-induced ferroelectric nanodomains in TTM and OAF at high fields (e.g., > 50 MV/m). It was observed that the Q_{31} could be enhanced by decreasing the dielectric nonlinearity from the RFE crystals. Combining both effects from D and Q_{31}, the overall

electrostrictive performance could be enhanced. i) At room temperature, the RFE terP-QSA60C film exhibited the highest electrostriction (3.6% at 200 MV/m), because it had relatively high D and Q_{31} (due to its low ferroelectric nonlinearity). ii) Above T_C, existing ferroelectric nanodomains in the nanocrystals disappeared. However, nanodomains could be induced by a high enough poling field (> 100 MV/m) in the paraelectric phase. Because of decreased ferroelectric nonlinearity (i.e., smaller nanodomains), the paraelectric terpolymer films were able to achieve high electrostrictive performance: ~5% at 200 MV/m.

The knowledge obtained from this study will help us design new RFE P(VDF-TrFE)-based terpolymers for further enhanced electrostrictive actuation. First, the large CTFE units should be more uniformly distributed in the polymer chains to divide up the ferroelectric domains into smaller ones. To achieve this, composition drift during radical copolymerization should be avoided, and continuous feeding of comonomers is an effective method.[36] Second, a new comonomer should be pursued to replace CTFE. Recently, a double-bond comonomer [from dehydrochlorination of P(VDF-CTFE)] was reported to enhance electroactuation.[37] It is possible to achieve better electrostrictive performance by exploring new terpolymers.

Supporting Information. The Supporting Information is available free of charge on the ACS Publications website at DOI: xxxxxxxxxxxxx.

1D SAXS profiles and correlation function analysis, FTIR spectra, nonlinear dielectric analyses for various terpolymer films at different temperatures, temperature-scan BDS results, and electrostrictive performance of terP-QSA60C at various temperatures.

Acknowledgments

L.Z. acknowledges financial support from National Science Foundation, Division of Materials Research, Polymers Program (DMR-2103196). H.H. acknowledges partial support by the National Natural Science Foundation of China (51873075). This research used the 11-BM CMS beamline of National Synchrotron Light Source-II (NSLS-II), Brookhaven National Laboratory (BNL), a U.S. Department of Energy User Facility operated for the Office of Science by BNL under Contract DE-SC0012704. The authors thank Dr. Masafumi Fukuto at NSLS-II of BNL for helping SAXS and WAXD experiments.

Conflict of Interest

The authors declare no conflict of interest.

References

1. Zhang, Q. M.; Huang, C.; Xia, F.; Su, J. Electric EAP. In *Electroactive Polymer (EAP) Actuators as Artificial Muscles: Reality, Potential, and Challenges*, 2nd ed., Bar-Cohen, Y., Ed.; SPIE Press: **2004**; Chapter 4, pp 89-139.
2. Li, F.; Jin, L.; Xu, Z.; Zhang, S. J. Electrostrictive Effect in Ferroelectrics: An Alternative Approach to Improve Piezoelectricity. *Appl. Phys. Rev.* **2014**, *1*, 011103.
3. Lehmann, W.; Skupin, H.; Tolksdorf, C.; Gebhard, E.; Zentel, R.; Krüger, P.; Lösche, M.; Kremer, F. Giant Lateral Electrostriction in Ferroelectric Liquid-Crystalline Elastomers. *Nature* **2001**, *410*, 447-450.
4. Zhang, Q. M.; Bharti, V.; Zhao, X. Giant Electrostriction and Relaxor Ferroelectric Behavior in Electron-Irradiated Poly(vinylidene fluoride-trifluoroethylene) Copolymer. *Science* **1998**, *280*, 2101-2104.

5. Chen, X.; Han, X.; Shen, Q. D. PVDF-Based Ferroelectric Polymers in Modern Flexible Electronics. *Adv. Electron. Mater.* **2017**, *3*, 1600460.

6. Han, X.; Chen, X.; Tang, X.; Chen, Y. L.; Liu, J. H.; Shen, Q. D. Flexible Polymer Transducers for Dynamic Recognizing Physiological Signals. *Adv. Funct. Mater.* **2016**, *26*, 3640-3648.

7. Liu, Y. M.; Ren, K. L.; Hofmann, H. F.; Zhang, Q. M. Investigation of Electrostrictive Polymers for Energy Harvesting. *IEEE Trans. Ultrason. Ferroelectr. Freq. Control* **2005***, 52,* 2411-2417.

8. Jean-Mistral, C.; Basrour, S.; Chaillout, J. J. Comparison of Electroactive Polymers for Energy Scavenging Applications. *Smart Mater. Struct.* **2010**, *19*, 85012.

9. Lallart, M.; Cottinet, P. J.; Guyomar, D.; Lebrun, L. Electrostrictive Polymers for Mechanical Energy Harvesting. *J. Polym. Sci., Part B: Polym. Phys.* **2012**, *50*, 523-535.

10. Lovinger, A. J. Radiation Effects on the Structure and Properties of Poly(vinylidene fluoride) and Its Ferroelectric Copolymers. In *Radiation Effects on Polymers*, Clough, R. L.; Shalaby, W., Eds.; American Chemical Society: Washington, DC, **1991**; Chapter 6, pp 84-100.

11. Yang, L.; Li, X.; Allahyarov, E.; Taylor, P. L.; Zhang, Q. M.; Zhu, L. Novel Polymer Ferroelectric Behavior via Crystal Isomorphism and the Nanoconfinement Effect. *Polymer* **2013**, *54*, 1709-1728.

12. Soulestin, T.; Ladmiral, V.; Dominguez Dos Santos, F.; Ameduri, B. Vinylidene Fluoride- and Trifluoroethylene-Containing Fluorinated Electroactive Copolymers. How Does Chemistry Impact Properties? *Prog. Polym. Sci.* **2017**, *72*, 16-60.

13. Wongwirat, T.; Zhu, Z.; Rui, G.; Li, R.; Laoratanakul, P.; He, H.; Manuspiya, H.; Zhu, L. Origins of Electrostriction in Poly(vinylidene fluoride)-Based Ferroelectric Polymers.

Macromolecules **2020**, *53*, 10942-10954.

14. Katsouras, I.; Asadi, K.; Li, M. Y.; van Driel, T. B.; Kjaer, K. S.; Zhao, D.; Lenz, T.; Gu, Y.; Blom, P. M.; Damjanovic, D.; Nielsen, M. M.; de Leeuw, D. M. The Negative Piezoelectric Effect of the Ferroelectric Polymer Poly(vinylidene fluoride). *Nat. Mater.* **2016**, *15*, 78-84.
15. Liu, Y.; Wang, Q. Ferroelectric Polymers Exhibiting Negative Longitudinal Piezoelectric Coefficient: Progress and Prospects. *Adv. Sci.* **2020**, *7*, 1902468
16. Strachan, A.; Goddard, W. A. Large Electrostrictive Strain at Gigahertz Frequencies in a Polymer Nanoactuator: Computational Device Design. *Appl. Phys. Lett.* **2005**, *86*, 83103.
17. Eury, S.; Yimnirun, R.; Sundar, V.; Moses, P. J.; Jang, S. J.; Newnham, R. E. Converse Electrostriction in Polymers and Composites. *Mater. Chem. Phys.* **1999**, *61*, 18-23.
18. Rui, G.; Huang, Y.; Chen, X.; Li, R.; Wang, D.; Miyoshi, T.; Zhu, L. Giant Spontaneous Polarization for Enhanced Ferroelectric Properties of Biaxially Oriented Poly(vinylidene fluoride) by Mobile Oriented Amorphous Fractions. *J. Mater. Chem. C* **2021**, *9*, 894-907.
19. Yang, L.; Tyburski, B. A.; Domingues Dos Santos, F.; Endoh, M. K.; Koga, T.; Huang, D.; Wang, Y.; Zhu, L. Relaxor Ferroelectric Behavior from Strong Physical Pinning in a Poly(vinylidene fluoride-*co*-trifluoroethylene-*co*-chlorotrifluoroethylene) Random Terpolymer. *Macromolecules* **2014**, *47*, 8119-8125.
20. Cheng, Z. Y.; Bharti, V.; Xu, T. B.; Wang, S.; Zhang, Q. M.; Ramotowski, T.; Tito, F.; Ting, R. Transverse Strain Responses in Electrostrictive Poly(vinylidene fluoride-trifluoroethylene) Films and Development of a Dilatometer for the Measurement. *J. Appl. Phys.* **1999**, *86*, 2208-2214.
21. Wongwirat, T.; Wang, M.; Huang, Y.; Treufeld, I.; Li, R.; Laoratanakul, P.; Manuspiya, H.; Zhu, L. Mesophase Structure-Enabled Electrostrictive Property in Nylon-12-based

Poly(ether-*block*-amide) Copolymers. *Macromol. Mater. Eng.* **2019**, *304*, 1900330.

22. Huang, Y.; Rui, G.; Li, Q.; Allahyarov, E.; Li, R.; Fukuto, M.; Zhong, G.-J.; Xu, J.-Z.; Li, Z.-M.; Taylor, P. L.; Zhu, L. Enhanced Piezoelectricity from Highly Polarizable Oriented Amorphous Fractions in Biaxially Oriented Poly(vinylidene fluoride) with Pure β Crystals. *Nat. Commun.* **2021**, *12*, 675.
23. Zhu, Z.; Rui, G.; Li, Q.; Allahyarov, E.; Li, R.; Soulestin, T.; Domingues Dos Santos, F.; He, H.; Taylor, P.; Zhu, L. Electrostriction-Enhanced Giant Piezoelectricity via Relaxor-Like Secondary Crystals in Extended-Chain Ferroelectric Polymers. *Matter* **2021**, under revision.
24. Chen, W.; Wunderlich, B. Nanophase Separation of Small and Large Molecules. *Macromol. Chem. Phys.* **1999**, *200*, 283-311.
25. Wunderlich, B. Reversible Crystallization and the Rigid-Amorphous Phase in Semicrystalline Macromolecules. *Prog. Polym. Sci.* **2003**, *28*, 383-450.
26. Hikosaka, M.; Sakurai, K.; Ohigashi, H.; Koizumi, T. Morphology of Extended Chain Single Crystals of Vinylidene Fluoride and Trifluoroethylene Copolymers. *Jpn. J. Appl. Phys.* **1993**, *32*, 2029-2036.
27. Ohigashi, H.; Omote, K.; Abe, H.; Koga, K. Chain Motions in the Paraelectric Phase in Single Crystalline Films of Vinylidene Fluoride and Trifluoroethylene Copolymer P(VDF/TrFE). *J. Phys. Soc. Jpn.* **1999**, *68*, 1824-1827.
28. Ohigashi, H.; Omote, K.; Gomyo, T. Formation of Single Crystalline Films of Ferroelectric Copolymers of Vinylidene Fluoride and Trifluoroethylene. *Appl. Phys. Lett.* **1995**, *66*, 3281-3283.
29. Tashiro, K., Crystal Structure and Phase Transition of PVDF and Related Copolymers. In *Ferroelectric Polymers: Chemistry, Physics, and Applications*, Nalwa, H. S., Ed.; Marcel

Dekker: New York, **1995**; Chapter 2, pp 63-182.

30. Tashiro, K.; Takano, K.; Kobayashi, M.; Chatani, Y.; Tadokoro, H. Structure and Ferroelectric Phase Transition of Vinylidene Fluoride-Trifluoroethylene Copolymers. 2. VDF 55% Copolymer. *Polymer* **1984**, *25*, 195-208.
31. Li, Y.; Ho, J.; Wang, J.; Li, Z.-M.; Zhong, G.-J.; Zhu, L. Understanding Nonlinear Dielectric Properties in a Biaxially Oriented Poly(vinylidene fluoride) Film at Both Low and High Electric Fields. *ACS Appl. Mater. Interfaces* **2016**, *8*, 455-465.
32. Tsang, C. H.; Shin, F. G. Simulation of Nonlinear Dielectric Properties of Polyvinylidene Fluoride Based on the Preisach Model. *J. Appl. Phys.* **2003**, *93*, 2861-2865.
33. Tashiro, K.; Nakamura, M.; Kobayashi, M.; Chatani, Y.; Tadokoro, H. Polarization Inversion Current and Ferroelectric Phase-Transition of Vinylidene Fluoride Trifluoroethylene Copolymer. *Macromolecules* **1984**, *17*, 1452-1455.
34. Jin Kim, K.; Reynolds, N. M.; Hsu, S. L., Spectroscopic Studies on the Effect of Field-Strength Upon the Curie Transition of a VDF/TrFE Copolymer. *J. Polym. Sci., Part B: Polym. Phys.* **1993**, *31*, 1555-1566.
35. Lee, J. S.; Prabu, A. A.; Kim, K. J.; Park, C. The Effect of an External Electric Field on Solid-State Phase Transition of P(VDF/TrFE)(72/28). *Fibers Polym.* **2007**, *8*, 456-462.
36. Huang, Y.; Xu, J.-Z.; Soulestin, T.; Domingues Dos Santos, F.; Li, R.; Fukuto, M.; Lei, J.; Zhong, G.-J.; Li, Z.-M.; Li, Y.; Zhu, L. Can Relaxor Ferroelectric Behavior be Realized for Poly(vinylidene fluoride-*co*-chlorotrifluoroethylene) [P(VDF-CTFE)] Random Copolymers by Inclusion of CTFE Units in PVDF Crystals? *Macromolecules* **2018**, *51*, 5460-5472.
37. Zhang, Z.; Wang, X.; Tan, S.; Wang, Q. Superior Electrostrictive Strain Achieved under Low Electric Fields in Relaxor Ferroelectric Polymers. *J. Mater. Chem. A* **2019**, *7*, 5201-5208.

TOC Graphic

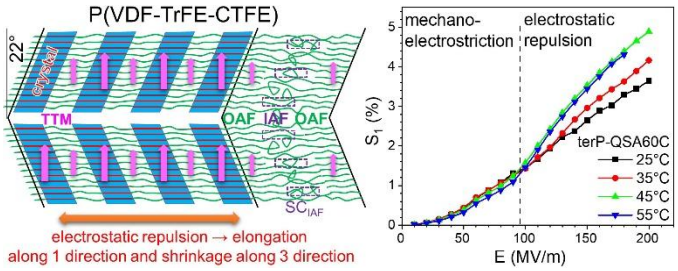
P(VDF-TrFE-CTFE)
22°
CF/Al
TTM
OAF IAF OAF
SC_IAF
electrostatic repulsion → elongation
along 1 direction and shrinkage along 3 direction
mechano-
electrostriction
electrostatic
repulsion
S1 (%)
E (MV/m)
terP-QSA60C
25°C
35°C
45°C
55°C